KeAi
CHINESE ROOTS
GLOBAL IMPACT

Contents lists available at ScienceDirect

Petroleum Science

journal homepage: www.keaipublishing.com/en/journals/petroleum-science



Original Paper

Experimental study of the characteristics of reverse fault slip induced by hydraulic fracturing



Xiao-Dong Wang ^{a,b}, Qian-Ting Hu ^{a,b}, Yong-Jiang Luo ^{a,b,*}, Bao-Cai Wang ^{a,b}, Sheng-Xian Zhao ^b, Shao-Jun Liu ^b, Yue Lei ^b

^a State Key Laboratory of Coal Mine Disaster Dynamics and Control, Chongqing University, Chongqing, 400044, China

ARTICLE INFO

Article history: Received 1 November 2024 Received in revised form 10 June 2025 Accepted 11 June 2025 Available online 14 June 2025

Edited by Yan-Hua Sun

Keywords: Hydraulic fracturing Induced reverse fault slip Physical test Simulation Safe injection distance

ABSTRACT

Hydraulic fracturing (HF) has achieved significant commercial success in unconventional oil and gas development. However, it has the potential to induce fault slip. This study investigates the physical mechanisms underlying potential fault slip triggered by HF operations under varying geological and operational constraints. First, we elucidate the relationship between the critical stress state and the elastic modulus of the fault, and refine a formula for the maximum crustal stress difference on critically stressed faults, including stress concentration, friction, and dip. Second, we compare the role of injected fluid in permeable faults with that in impermeable faults, and demonstrate that fault slips can be triggered by a combination of friction decrease and pore pressure increase, even after ceasing injection. Specifically, we reveal that friction decline dominates induced fault slip on high permeable and hydraulically connected fault. Third, based on experimental results and theoretical analysis, we quantify the influence region of stress transfer under different conditions of well location and injection pressure. The results reveal that the elastic modulus of the fault controls the stress concentration on the fault plane. The dip of the fault and the stress concentration jointly determine the maximum crustal stress difference required for failure in critically stressed reverse faults. Thus, our study is more accurate in estimating the proximity of the in-situ stress to the critical state, compared with traditional methods. For critical reverse faults, the risk of induced slip is positively correlated with both injection pressure and friction of fault plane. When the injection pressure (P_1) is 100 MPa and the friction (μ) is 0.8, the safe distance from injection point to critically stressed faults along the direction of maximum principal stress and maximum principal stress (d_H and d_V) should exceed 25 and 18 times as the hydraulic fracture halflength. When $P_{\rm I}$ is 100 MPa and μ is 0.6, $d_{\rm H}$ and $d_{\rm V}$ are 23 and 17 times as the hydraulic fracture halflength, respectively. When P_1 is 60 MPa and μ is 0.6, d_H and d_V are 18 and 13 times as the hydraulic fracture half-length, respectively. The works enhance our understanding of HF-induced fault slip and potentially guide designs of the shale gas well location and trajectory for safer production.

© 2025 The Authors. Publishing services by Elsevier B.V. on behalf of KeAi Communications Co. Ltd. This is an open access article under the CC BY-NC-ND license (http://creativecommons.org/licenses/by-nc-nd/4.0/).

1. Introduction

Since hydraulic fracturing (HF) has emerged as the most efficient method for enhancing reservoir permeability and creating complex fracture networks that serve as flow channels for

E-mail address: luoyj16@cqu.edu.cn (Y.-J. Luo).

Peer review under the responsibility of China University of Petroleum (Beijing).

hydrocarbons, it has been widely utilized in unconventional oil & gas development (Eyre et al., 2019a; Rezlerova et al., 2021; Yehya et al., 2022; Gao et al., 2024; Li et al., 2024). Concurrently, HF crack propagation and sufficient fluid injection alter in-situ stress and increase pore pressure (Bao and Eaton, 2016; Benson et al., 2020; Villa and Singh, 2020). When these coupled fluid flow and deformation processes interact with existing fault systems, they may intensify fault-related hazard (Kim et al., 2018; Eyre et al., 2019b; Li et al., 2022; Xiao et al., 2023).

Since 2010, several suspected HF induced fault slip events were detected (Schultz et al., 2017; Atkinson et al., 2020; Li et al., 2023;

^b School of Resources and Safety Engineering, Chongqing University, Chongqing, 400044, China

^{*} Corresponding author. State Key Laboratory of Coal Mine Disaster Dynamics and Control, Chongqing University, Chongqing, 400044, China.

Hu et al., 2018; Tan et al., 2020; Sheng et al., 2022), as shown in Fig. 1. Understanding these processes is crucial for developing strategies to prevent or mitigate HF-induced fault slip.

Based on the Coulomb failure criterion, several mechanisms have been established to explain fault slip induced by hydraulic fracturing (HF) operations. These include pore pressure diffusion (Ge and Saar, 2022; Stokes et al., 2023), the poroelastic stress effect (Deng et al., 2016; Fan et al., 2019), and aseismic slip (Guglielmi et al., 2015; Eyre et al., 2019a). The Coulomb failure stress (CFS) increases with rising pore pressure due to fluid injection, a phenomenon known as the pore pressure diffusion effect. This mechanism is typically regarded as the dominant factor for reactivation, particularly in permeable reservoirs (Goebel and Brodsky, 2018). The influence of pore pressure can be observed at increasing distances and over extended periods following injection. Therefore, it is not suitable for explaining induced events that occur at the moment of fracking, such as those noted during the Preston New Road PNR-1z hydraulic fracturing operation in the United Kingdom (Kettlety and Verdon, 2021). During HF operations, the tensile opening of cracks induces geomechanical deformations and creates perturbations in the in-situ stress state. When these perturbations reduce normal stress (σ_n) and/or increase shear stress (τ), fault reactivation occurs—a process known as the poroelastic stress effect. Induced events occurring shortly after injection may be triggered at the speed of compressional waves (Deng et al., 2016). To determine the triggering conditions associated with the poroelastic stress effect and to elucidate the spatiotemporal patterns of fault reactivation sequences, several models have been developed and applied in forecasts of induced fault reactivation (Meier et al., 2014; Zeng and Guo, 2016; Ji et al., 2022). The fault activity interaction can further facilitate the HF induced events (Zhang et al., 2022; Moein et al., 2023). Each of these mechanisms alone may not fully account for the physical processes of induced fault slip (Anyiam et al., 2024; Zhang et al., 2022).

Data from reported induced fault slip events provides an opportunity to explore induced fault slip mechanisms and hazard identification (Goebel and Brodsky, 2018; Kemna et al., 2022; Zhang et al., 2025). Spatial data of 18 global induced cases shows a clear correlation between distance and delay (Goebel and Brodsky, 2018). The geological parameters, such as the target formation and its thickness, are most influential to the fault activation in the Kiskatinaw area in northeast British Columbia, the

operational parameters are second (Kemna et al., 2022). Limited by the experimental conditions, the number of physical experiments is small and concentrated on the research of poroelastic stress effect (Dutler et al., 2021) and aseismic slip (Guglielmi et al., 2015; Bhattacharya and Viesca, 2019). Pore pressure increase is consistently observed in physical simulations at the Grimsel Test Site (Dutler et al., 2021). Injection first caused fault aseismic slip near the wells, and the development of aseismic slip then led to largerscale fault slip, which transition was independent of any pressure change (Guglielmi et al., 2015). The induced fault slip front diffused faster and farther than the pressurized pore fluid (Bhattacharya and Viesca, 2019). The numerical simulation studies also analyze the control factors inducing fault slip based on a special geological background (Wang et al., 2020, 2021; Leng and Hu, 2024). The M_W 4.6 event on August 17, 2015 in Canada occurred on a pre-existing fault and its maximum magnitude was controlled by geological structural conditions (Wang et al., 2020). The subsequent numerical simulation results show that there is likely to be a high-permeability fluid channel between the fracturing fluid injection zone and the target fault (Wang et al., 2021). The connecting zone of Δ CFS high value area is formed in the crystalline basement between the adjacent faults (Leng and Hu, 2024).

Research on predicting and assessing HF-induced fault slip is still in its early stages (Gao et al., 2024). Most existing studies are either qualitatively descriptive or focused on specific geological contexts, lacking systematic quantitative analyses (Schultz et al., 2021: Reves et al., 2022). While the connections between HF operations and fault reactivation are evident, the underlying physical processes that trigger this reactivation remain poorly understood (Sun et al., 2024). In particular, descriptions of the spatiotemporal evolution of injection-induced fault reactivation primarily rely on fault slip migration or surface geodetic observations, as continuous in-situ measurements are lacking (Kettlety and Verdon, 2021). Consequently, the conditions that trigger induced fault slip remain contentious. Firstly, fault criticality is a poorly constrained parameter that determines the minimum Δ CFS threshold (Kettlety et al., 2020). Secondly, the friction along the fault plane is often assumed to be constant, which does not accurately reflect reality but significantly influences induced fault reactivation. Thirdly, the connection between fault slip risk and operational parameters is partly understood, the effective disturbance range of poroelastic stress within a given Δ CFS threshold remains uncertain

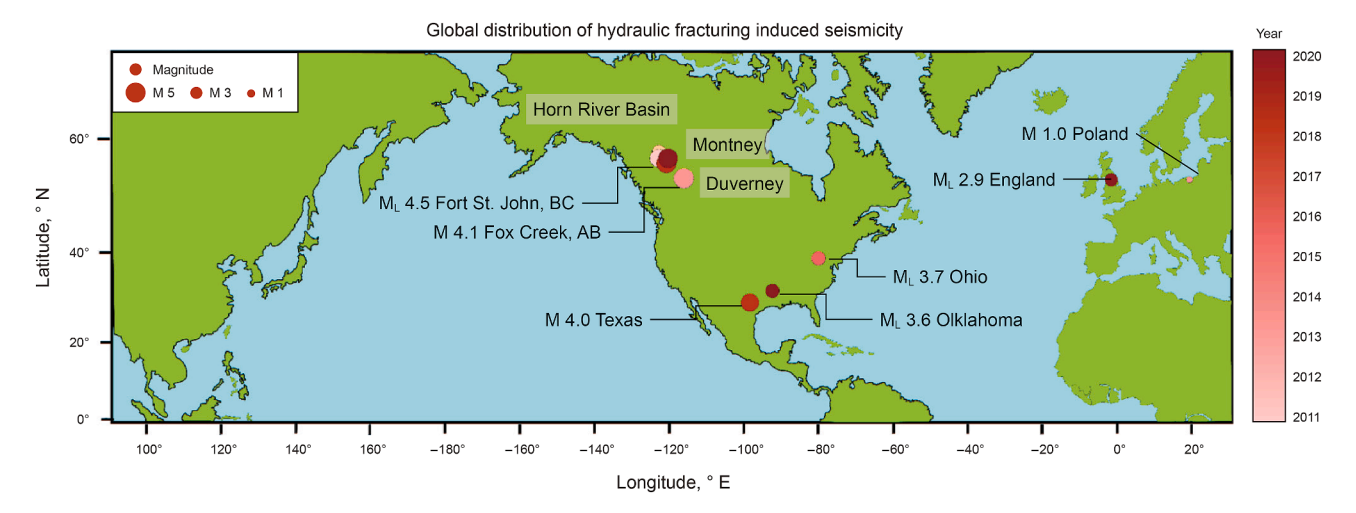


Fig. 1. Global distribution of hydraulic fracturing induced fault slip (adapted from Atkinson et al., 2020). Color bar shows the year of events, and the size of circle represents the magnitude scale.

(Kemna et al., 2022). Lastly, a significant gap we face is not knowing which faults are hazardous, lacking detailed research on the mechanical properties of the faults (Gao et al., 2024).

In this study, we employ a series of meter-scale true triaxial physical tests and rock failure process analysis (RFPA) numerical simulation to quantitatively describe the response of stress change and pore pressure change on fault plane pre- and post-injection and achieve the following objectives: (1) propose an improved formula to determine the critical stress states of faults with stress concentration, dips, cohesion and friction of fault plane; (2) propose that friction decline on hydraulically connected faults is another mechanism of HF-induced fault reactivation; (3) characterize the evolution of fault plane friction under different mechanisms; (4) theoretically calculate the effective influence range of poroelastic stress effects. Our findings contribute to developing safer hydraulic fracturing operation plans.

2. Materials and methods

2.1. Experimental apparatus

The experimental apparatus includes a large scale true triaxial loading system, a TC-260L pump injection system, and a DH5922D dynamic signal acquisition and analysis system, as shown in Fig. 2. The large scale true triaxial loading system integrates both a loading system and an indenter data acquisition system. The dimension of the sample compartment is 1 m \times 0.5 m \times 0.5 m $(x \times y \times z)$, with a maximum load capacity of 15 MPa in the x, y, and z directions. Loads are measured using strain gauge load cells with a resolution of 0.1 kN. The maximum displacement is 0.3 m \times 0.1 m \times 0.1 m ($x \times y \times z$), with a precision of \pm 0.1%. Data are recorded using an analog-to-digital converter at a sampling rate of 10 kHz, and subsequently averaged for storage rates of 1, 10, and 100 Hz. The TC-260L pump injection system features an integrated water tank and fracturing pump, capable of operating in both constant flow and constant pressure modes. The system supports a flow rate range of 0.1-100 mL/min and a maximum pressure of 60 MPa. The DH5922D dynamic signal acquisition and analysis system can simultaneously record the data of stress sensors and pore pressure sensors, with a precision of $\pm 0.5\%$.

2.2. Sample preparation

We use one rock material and three kinds of fault materials to investigate the role of the elastic modulus, friction, and permeability of fault in controlling induced fault reactivation. We made

standard samples of different materials to test the mechanical properties. Uniaxial compressive strength and triaxial compression strength were tested using rock mechanics test system MTS 815 (the instrument and operation are described in Liu et al., 2024) to obtain the elasticity modulus, internal friction angle, and Poisson's ratio of different materials. The frictions of the faults are tested using self-developed coal rock shear-flow coupling test device (the instrument and operation are described in Xu et al., 2015). All the tests are completed in the State Key Laboratory of Coal Mine Disaster Dynamics and Control, Chongqing University. The major parameters are shown in Table 1.

A total of 17 samples are prepared. One sample before and after injection is shown in Fig. 3.

The fault material, locations of sensors, and injection points are detailed in Table 2 and illustrated in Fig. 4. Here, $\sigma_{\rm crit}$ presents the critical stress, defined as the value of $\sigma_{\rm X}$ at the moment of fault slip starting. Tests 1–5 are conducted to acquire the critical stress under different dips and fault materials. Tests 6–8 investigate the response of friction decline on induced fault slip, when the fault absorbed a significant amount of water. Test 9 aims to investigate the effect of pore pressure diffusion on induced fault slip and evolution of friction. Tests 10–17 explore the response of stress transfer on induced fault slip of hydraulic isolated fault.

2.3. Experimental parameters

When the physical experimental conditions cannot meet the prototype conditions, such as tri-axial stress, it is reasonable to scale the stress conditions by the similarity criterion. And the primary similarity parameters dominating the rationalization of physical tests results are stresses and mechanical properties (Liu et al., 2023). The mechanical properties of fault and dips are the variable factors in our study, so we only refer to the in-situ stress of the prototype to set the boundary stress conditions of our tests. The stress state of some reverse faults where induced slip occurs are listed in Table 3. The value of $\sigma_{2(\text{eff})}$: $\sigma_{3(\text{eff})}$ is taken as 1.6. In our tests, σ_{x} , σ_{y} , and σ_{z} take place of σ_{1} , σ_{2} , and σ_{3} . In order to allow enough increment of σ_{x} to meet the critical stress state (shear failure of the fault), σ_{z} and σ_{y} are taken as 2.5 and 4 MPa, respectively.

2.4. Test procedure

Four loading steps are applied in the critical stress tests (Tests 1–5). Firstly, exert minimal restraining forces (20 kN) in all three directions to immobilize the samples. Secondly, set indenters X_3

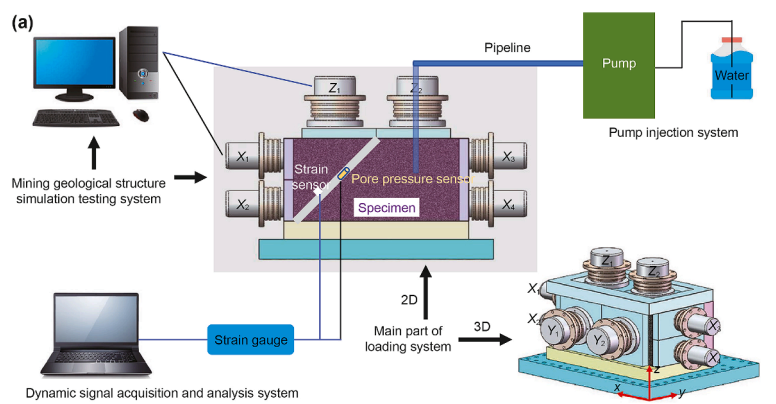




Fig. 2. Experimental apparatus.

Table 1 Major parameters of the samples.

| Material | Elastic modulus E, GPa | Internal friction angle φ , $^\circ$ | Permeability | Friction μ | Poisson's ratio v |
|-------------------------------|------------------------|--|---------------------------|----------------|-------------------|
| Rock material | 3.87 | 39.4 | Impermeable | 1 | 0.22 |
| Fault material-1# | 0.08 | 32.5 | Permeable and hydrophilic | 0.64 | 0.25 |
| Fault material-2 [#] | 0.32 | 30.2 | Impermeable | 0.62 | 0.24 |
| Fault material-3# | 0.79 | 27.8 | Impermeable | 0.60 | 0.23 |







Fig. 3. A sample before and after injection.

Table 2 Test parameter settings.

| Test No. | Dip angle, ° | Fault material | Injection point | Pore pressure sensors | σ_{χ} |
|----------|--------------|----------------|-----------------|-----------------------|------------------------------|
| 1 | 15 | 1# | 1 | 1 | Acquire $\sigma_{ m crit}$ |
| 2 | 30 | 1# | | | - |
| 3 | | 2# | | | |
| 4 | | 3# | | | |
| 5 | 45 | 1# | | | |
| 6 | 45 | 1# | 1 | ✓ | $0.80\sigma_{ m crit}$ |
| 7 | | | | | $0.90\sigma_{\mathrm{crit}}$ |
| 8 | | | | | $0.95\sigma_{\mathrm{crit}}$ |
| 9 | | 2# | | | $0.80\sigma_{ m crit}$ |
| 10 | 30 | 1# | 1 | ✓ | $\sigma_{ m crit}$ |
| 11 | | | 2 | | $\sigma_{ m crit}$ |
| 12 | | | 3 | | $\sigma_{ m crit}$ |
| 13 | | | 4 | | $\sigma_{ m crit}$ |
| 14 | 45 | 1# | 2 | √ | $0.95\sigma_{ m crit}$ |
| 15 | | | 2 | | $\sigma_{ m crit}$ |
| 16 | | | 3 | | $0.95\sigma_{\mathrm{crit}}$ |
| 17 | | | 3 | | $\sigma_{ m crit}$ |

and X_4 keeping displacement constant, while the other indenters are controlled by stress. Then, σ_X , σ_y , and σ_Z are simultaneously loaded at the rates of 0.002, 0.0016, and 0.001 MPa/s, respectively, where, σ_y and σ_Z are set to remain constant after reaching the

preset confining pressure. After that, σ_X is continually loaded until fault slip occurs. The value of σ_X at the onset of slip is recorded as σ_{crit} .

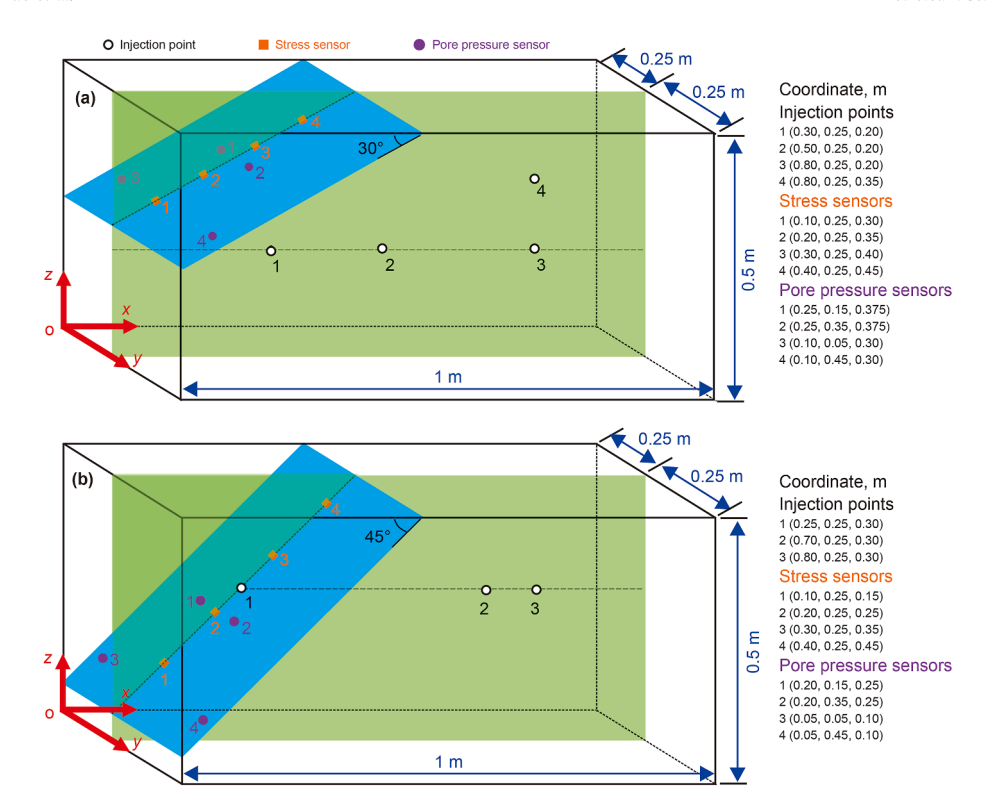


Fig. 4. Locations of injection points, stress sensors, and pore pressure sensors.

 Table 3

 Ratio of effective in-situ stress around the fault plane.

| Study area | Depth, m | σ _{1(eff)} :σ _{2(eff)} :σ _{3(eff)} | References | |
|------------------------|-----------|---|-------------------------|--|
| Southeast France Basin | 282 | 2.00:1.67:1.00 | Guglielmi et al. (2015) | |
| Shangluo area | 2300-3000 | 2.32:-:1.00 | Lei et al. (2017) | |
| YZ fault area | 2500 | 2.18:1.58:1.00 | Hu et al. (2018) | |
| N201 well | 2000 | 2.82:1.55:1.00 | Sun et al. (2024) | |

Table 4 Steps of hydraulic fracturing tests.

| Step | Step Tests | | | | | | |
|------|--|---|--|--|--|--|--|
| | 6–8 | 9 | 10–17 | | | | |
| 1 2 | Same as Test 1. | Same as Test 6. | Same as Test 6. | | | | |
| 3 | Set σ_x , σ_y , and σ_z remain constant after reaching the preset values listed in Table 2. | | | | | | |
| 4 | Inject continuously at a rate of 100 mL/min. | | Inject at stepwise increasing pressures (3, 4, 5, 6, 7 MPa,) until the rock cracks. | | | | |
| 5 | Stop injection after 40 min, then remain the pressurization for 30 min. $ \\$ | Stop injection after induced fault slip lasting 10 min. | Remain the fracture initiation pressure until the HF crack reach the edge of the sample. | | | | |

The steps of hydraulic fracturing tests (Tests 6–17) are shown in Table 4. In tests 10–17, we set injection pressure incremented step by step for the following reasons. First, excessive pressure will break the sample instantaneously, which lead to the data of sensors deficiencies. This disadvantage could be effectively avoided by injection pressure incremented step by step. Second, the change of injection pressure and fracture pressure is positively correlated with the pump injection rate (Shao et al., 2020). Third, our objective is to investigate the stress transfer effect directly affected by the pressure of crack expansion. So, the setup is reasonable.

2.5. Models

Based on the theory in "Fundamentals of Rock Mechanics" (Jaeger et al., 2007), the normal stress (σ_n) and shear stress (τ) on the fault plane can be expressed as

$$\sigma_{\rm n} = \frac{\sigma_1 + \sigma_3}{2} + \frac{\sigma_1 - \sigma_3}{2} \cos 2\left(\frac{\pi}{2} - \alpha\right) \tag{1}$$

$$\tau = \frac{\sigma_1 - \sigma_3}{2} \sin 2\left(\frac{\pi}{2} - \alpha\right) \tag{2}$$

where σ_1 and σ_3 are the maximum and minimum principal stresses, respectively; α is the fault dip.

Fault shear failure follows Mohr–Coulomb failure criterion (Labuz and Zang, 2012). The proximity of the in-situ stress state to the fault shear failure can be expressed in terms of the Coulomb failure stress (CFS):

$$CFS = \tau - \mu(\sigma_n - p) - C \tag{3}$$

where p is the pore pressure; μ is the friction; and C is the cohesion of the fault plane. If a perturbation causes a positive Δ CFS, the likelihood of fault shear failure increases.

Stress change at a certain location near the hydraulic fracture during the process of hydraulic fracture expansion can be expressed as follows (Zeng and Guo, 2016),

criterion is the first damage threshold, which primarily determines whether a crack has been initiated, as shown in Eq. (5).

$$\varepsilon_{\rm t} \le \frac{\sigma_{\rm t}}{F}$$
 (5)

where ε_t is the tensile strain, dimensionless; σ_t is the strength of extension, MPa; E is the elastic modulus, MPa.

The Mohr–Coulomb criterion is the second damage threshold, which is exactly the principle followed by fault shear failure in the absence of tensile damage, as shown in Eq. (6).

$$\sigma_1 - \sigma_3 \frac{1 + \sin\varphi}{1 - \sin\varphi} \ge \sigma_{\rm C} \tag{6}$$

where $\sigma_{\rm C}$ is the uniaxial compressive strength; φ is the internal

$$\begin{cases} \Delta \sigma_{z} = -p_{s} \frac{r}{a} \left(\frac{a^{2}}{r_{1} r_{2}}\right)^{3/2} \sin\theta \sin\frac{3}{2} (\theta_{1} + \theta_{2}) - p_{s} \left[\frac{r}{\sqrt{r_{1} r_{2}}} \cos\left(\theta - \frac{1}{2}\theta_{1} - \frac{1}{2}\theta_{2}\right) - 1\right] \\ \Delta \sigma_{x} = p_{s} \frac{r}{a} \left(\frac{a^{2}}{r_{1} r_{2}}\right)^{3/2} \sin\theta \sin\frac{3}{2} (\theta_{1} + \theta_{2}) - p_{s} \left[\frac{r}{\sqrt{r_{1} r_{2}}} \cos\left(\theta - \frac{1}{2}\theta_{1} - \frac{1}{2}\theta_{2}\right) - 1\right] \\ \Delta \sigma_{y} = \nu(\Delta \sigma_{x} + \Delta \sigma_{z}) \\ \Delta \tau_{xz} = -p_{s} \frac{r}{a} \left(\frac{a^{2}}{r_{1} r_{2}}\right)^{3/2} \sin\theta \cos\frac{3}{2} (\theta_{1} + \theta_{2}) \end{cases}$$

$$(4)$$

where a is the hydraulic fracture half length, m; p_s is the pressure on the hydraulic fracture surface, MPa. p_s is close to the injection pressure, without considering the loss of crack propagation. The geometric relationship of $r(r, r_1, r_2)$ and $\theta(\theta, \theta_1, \theta_2)$ is shown in Fig. 5.

3. Numerical simulation

Limited by the small value of fault elastic modulus in the samples, the applicability of physical tests is poor. Hence, we use numerical simulation with wider range of elastic modulus of fault to study the stress concentration on the fault plane and critical state.

The RFPA software is programmed to simulate discontinuous mechanical problems by reducing parameters after element failure through continuum mechanics, and calculates the damage thresholds using two criterion. The maximum tensile strain friction angle.

We build the field-scale 3-D models of faults that strike N-S (north to south; parallel to the y direction) and dip to the west (negative x direction). The models are equally divided into $100 \times 50 \times 50$ orthogonal hexahedral elements, each with an edge length of 10 mm, an example is shown in Fig. 6.

The boundary conditions matched those of the physical tests. The primary parameters which reference the parameters of the physical samples are shown in Table 5. Among them, the internal friction angle and Poisson's ratio of the numerical simulation are set according to the parameters of samples in the physical tests, the elastic modulus of fault is widely taken in the range of less than rock to study the influence of fault elastic modulus on stress concentration.

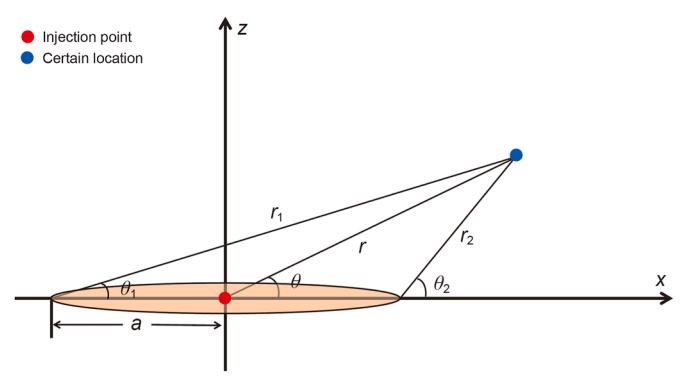


Fig. 5. The geometric relationship (modified from Zeng and Guo, 2016).

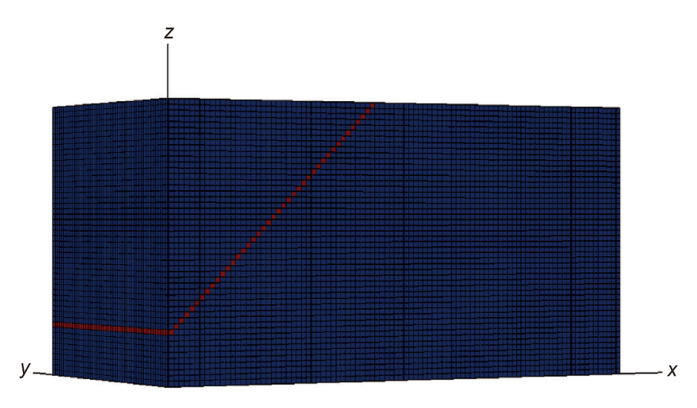


Fig. 6. Numerical simulation meshing of 45° dip fault.

Table 5Major parameters in numerical model.

| Material | Elasticity modulus E, GPa | Internal friction angle φ , $^\circ$ | Poisson's ratio ε | Fault dip α , $^{\circ}$ |
|----------------|--|--|-------------------------------|---------------------------------|
| Rock material | 3.87 | 40 | 0.22 | _ |
| Fault material | $0.08, 0.32, 0.79, 3.87\times 0.0025/0.0125/0.025/0.05/0.1/0.2/0.3/0.4/0.5/0.6/0.7/0.8/0.9*$ | 30 | 0.25 | 15, 30, 45 |

Note: * indicates that the value of fault material is the size of rock material multiplied by a coefficient, for example, $3.87 \text{ GPa} \times 0.0025 = 0.009675 \text{ GPa}$; $3.87 \text{ GPa} \times 0.8 = 3.096 \text{ GPa}$; $3.87 \text{ GPa} \times 0.9 = 3.483 \text{ GPa}$.

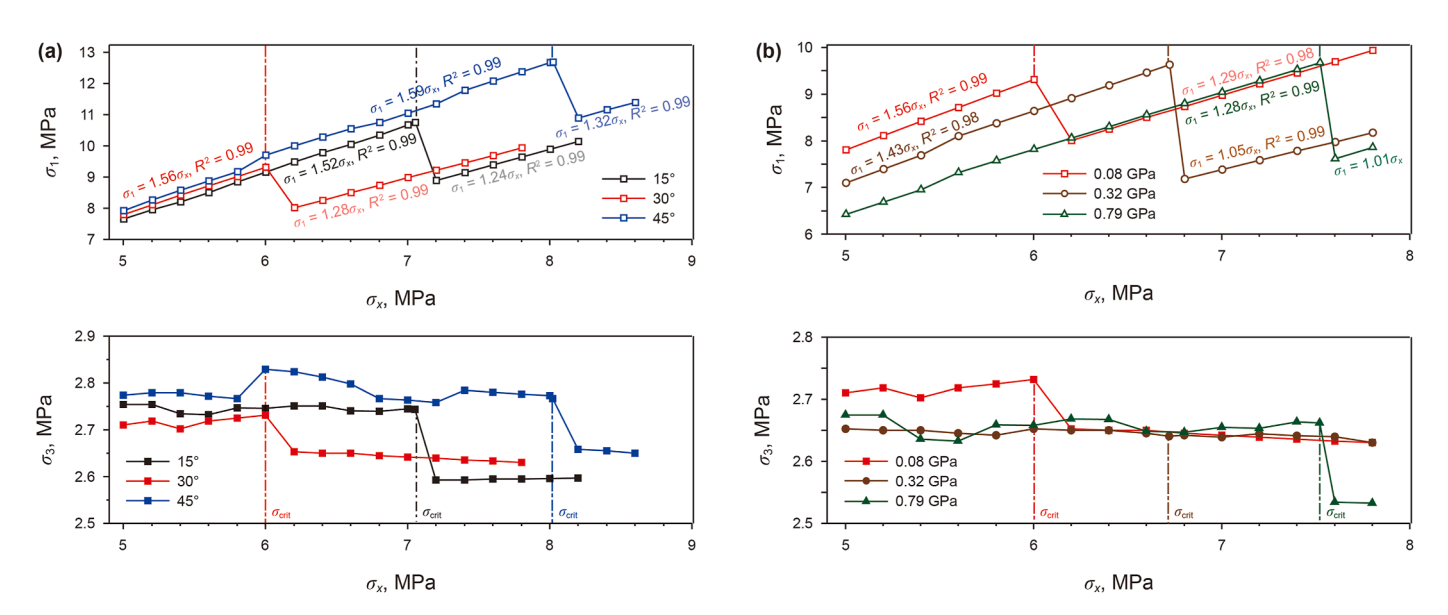


Fig. 7. The evolution of σ₁ and σ₃ on fault plane in physical tests. (a) Comparison of dips (results of Tests 1–3). (b) Comparison of fault elasticity modulus (results of Tests 2, 4, 5).

4. Results

4.1. Fault critical stress state

In physical tests, before fault slip occurs, the concentration of σ_1 on the fault plane remains nearly constant, the concentration of σ_3 on the fault plane is almost negligible (Fig. 7). When the elasticity modulus of the faults (E_f) is 0.04 GPa, the fitted concentrations of σ_1 are 1.52, 1.56, and 1.59, the $\sigma_{\rm crit}$ are 6.00, 7.05, and 8.02 MPa, corresponding dips are 15°, 30°, and 45° (Fig. 7(a)). When the dip is 30°, the fitted concentrations are 1.56, 1.43, and 1.05, the $\sigma_{\rm crit}$ values are 6.00, 6.72, and 7.52 MPa, corresponding E_f are 0.08, 0.32, 0.79 GPa (Fig. 7(b)). Once slip occurs, the concentration of σ_1 on the fault plane is rapidly released (Fig. 7).

The results of numerical simulation are in good agreement with those of physical tests, including the concentration of σ_1 (Fig. 8(a) and (b)) and the maximum crustal stress difference (σ_1/σ_3) on critical stress fault (Fig. 8(c) and (d)).

In numerical simulation, obviously, the concentration of σ_1 is less influenced by dips, but dominated by the elasticity modulus of the faults, which is consistent with the results of the physical tests. As the E_1/E ratio increases, the concentration of σ_1 on the fault plane gradually converges to 1 (Fig. 9(a)). Moreover, the ratio of regional maximum to minimum principal stress (σ_1/σ_3) at the critical stress state increases as the E_1/E increases (Fig. 9(b)), which significantly differs from the result ($\sigma_1/\sigma_3 = 3.35$) calculated by the friction-only model of (Hu et al., 2018).

4.2. Role of fluid in hydraulically connected fault

This section focuses on the evolution of pore pressure (p), effective principal stress ($\sigma_{\rm eff}$), shear stress (τ), and friction

throughout the hydraulically connected faults pre- and postinjection. To exclude the effect of stress transfer, injection holes are set on the fault plane (injection point 1[#] in Fig. 4(b)). Parameters of these physical tests are presented in Table 2.

For the permeable faults (Tests 6–8), all the positive pressure changes (Δp) are less than 0.1 MPa after injection (Fig. 10(a)–(c)). Water absorption reduces the elastic modulus of the faults, which leads to a minor increase in $\sigma_{\rm eff}$ (Fig. 10(e)–(g)) and τ before fault slip occurrence (Fig. 10(i)–(k)). When σ_x is 0.80 σ_{crit} , no fault slip occurs. When σ_X is 0.90 σ_{crit} , the fault slides 0.018 mm at an average rate of 0.18 μ m/s after shut-in. When σ_X is 0.95 σ_{crit} , the fault slides 0.26 mm at an average rate of $2.58 \mu \text{m/s}$ during injection. It means that the closer the regional stress is to the critical stress state, the longer and faster the fault slides. If the friction remains constant after the faults absorbing plenty of water, all the values of CFS calculated by Eq. (1) are less than 0, contradicting the observed fault slip (Fig. 10(p)). Apparently, the above assumption is unreasonable. The friction of the fault plane is measured by analyzing forces on an inclined plane using a spring-loaded dynamometer, and the temporal evolution of friction at different injection volumes is shown in Fig. 11. Based on these results, the temporal evolution of CFS are calculated and demonstrated (Fig. 10(m)-(o)). CFS > 0 across the entire fault plane is necessary for fault slip (Fig. 10(m) and (p)). After the slip ends, both $\sigma_{\rm eff}$ and τ decrease, the fault locks again.

For impermeable fault (Test 9), the evolution of $\sigma_{\rm eff}$ on fault plane is inversely related to pore pressure (Fig. 10(d) and (h)), which indicates that pore pressure is the dominant factor for the induced fault slip. Specifically, the change in shear stress ($\Delta \tau$) is less than 0.2 MPa (Fig. 10(l)), which is significantly smaller than the changes in Δp (2.4 MPa) and $\Delta \sigma_{\rm eff}$ (2.2 MPa) (Fig. 10(d) and (h)). Slip initiates at a pressure of about 1.0 MPa (S_0 in Fig. 10(p)). From

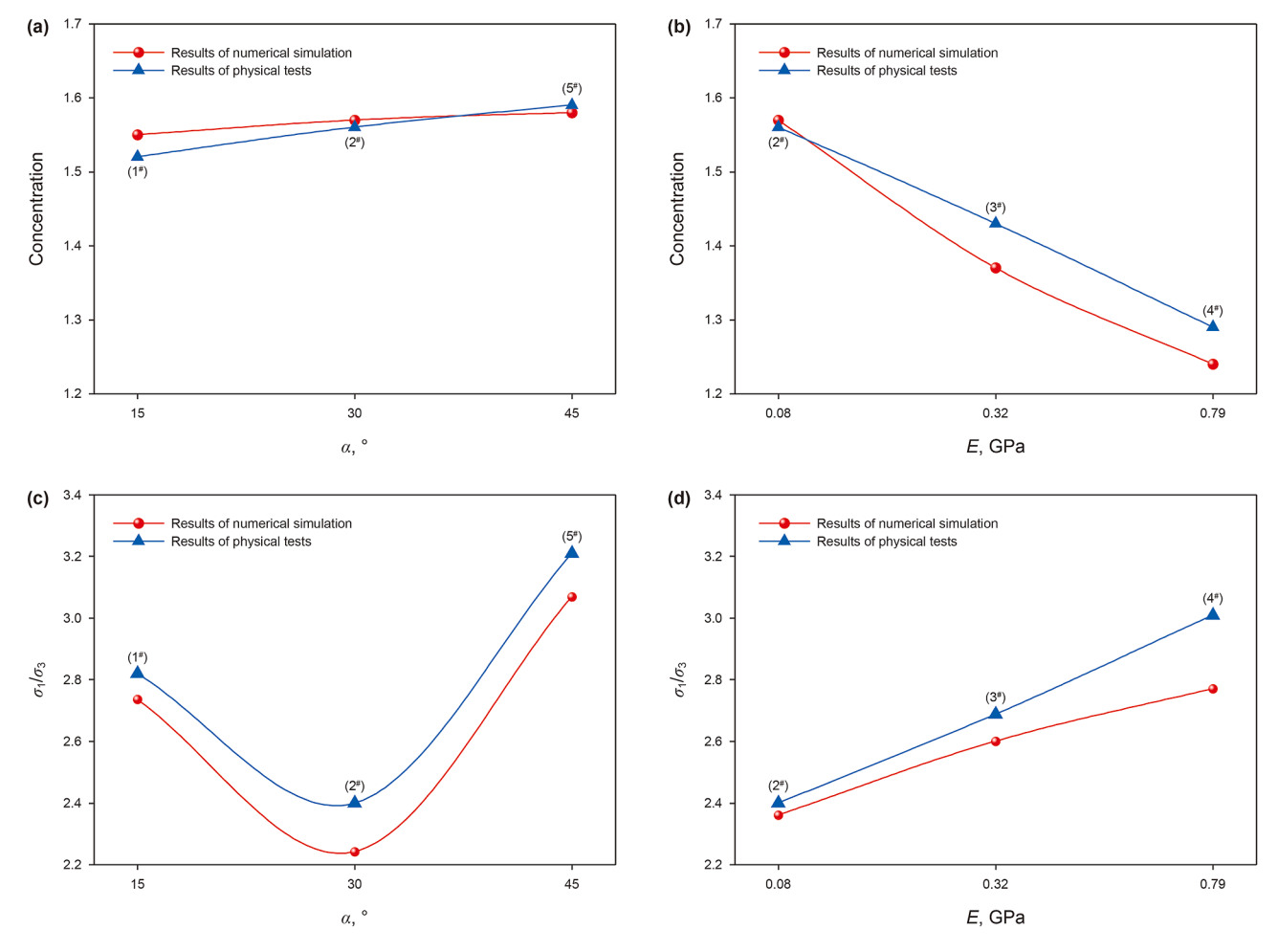


Fig. 8. Numerical simulation verification (using results of Tests 1–5).

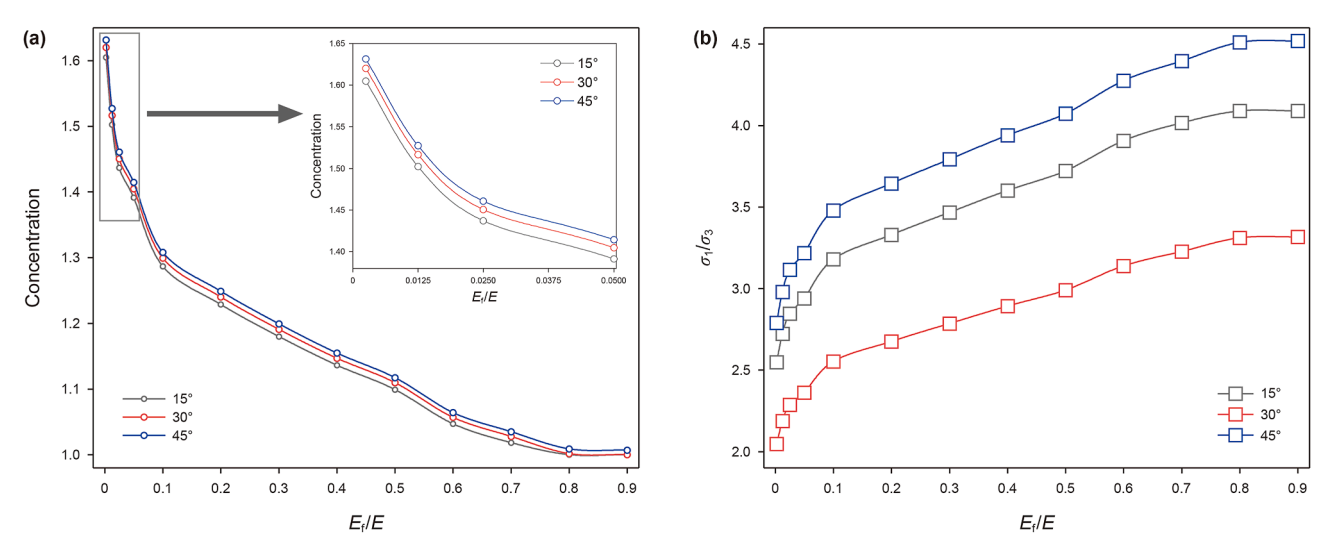


Fig. 9. The stress characteristic on fault plane in numerical simulation. (a) The concentration versus the elastic modulus of faults. (b) The ratio of regional maximum to minimum principal stress versus the elastic modulus of faults.

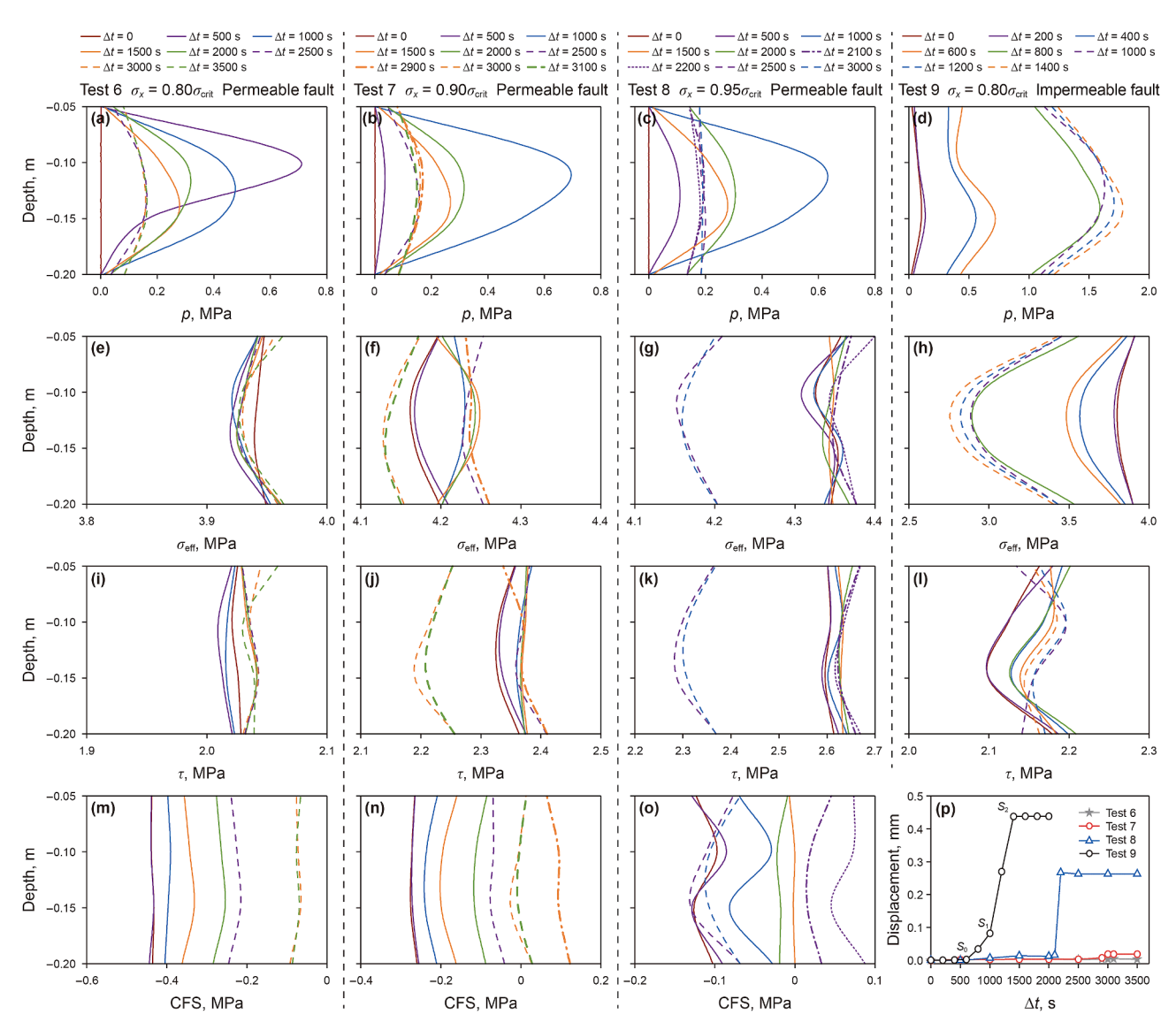


Fig. 10. Response on faults, the first three columns are hydrophilic faults, while the fourth column are for impermeable fault (except Fig. 10(p)). Temporal evolution of pore pressure (a)–(d), effective normal stress (e)–(h), shear stress (i)–(l), and CFS (m)–(o). (p) Temporal evolution of slip.

 S_0 to S_1 , the fault slides 0.08 mm. From S_1 to S_2 , the fault slides 0.35 mm.

4.3. Stress transfer on hydraulic isolated fault

To investigate the relationship between stress perturbation and spatial position, we design comparison tests with variable injection locations (Table 2, Fig. 4). The directions of the maximum and minimum horizontal stresses are set to be orthogonal and parallel to the fault strike (Fig. 4), facilitating a symmetric distribution of horizontal stress components relative to the fault orientation during injection. In our tests, the original pore pressure in samples is 0. In cases where no crack connects to the fault, the pore pressure in the fault region remains constant, with the poroelastic effect evident manifested solely as stress transfer through the rock framework.

In sample with 30° fault scenario, when the injection hole lies directly beneath the fault (injection point 1[#] in Fig. 4(a)), slip is unlikely to occur even under critical stress conditions (Fig. 12(m)), because stress transfer leads to a significant positive $\Delta \sigma$ (Fig. 12(a)),

so that Δ CFS throughout the faults is almost exclusively negative (Fig. 12(i)). When the injection point is 2[#] in Fig. 4(a), a minor increase in CFS is swiftly followed by a negative response (Fig. 12(j) and (n)) during injection. Accordingly, the fault displacement remains stable after a slight increase (Fig. 12(m) and (n)). These phenomena suggest that when hydraulic fractures extend below the reverse fault, the CFS on the fault plane experiences a negative change, reducing the likelihood of fault slip. When injection point is far from the fault (injection points 3[#] and 4[#] in Fig. 4(a)), crack extension causes a negative $\Delta \sigma$ (Fig. 12(c) and (d)), positive $\Delta \tau$ (Fig. 12(g) and (h)), and positive Δ CFS (Fig. 12(k) and (l)) on the fault planes. The Δ CFS significantly correlates with the proximity of the injection points to the fault. Post-slip, CFS drops below 0, which indicates a lower likelihood of fault slip than pre-injection (line $\Delta t = 300$ s in Fig. 12(j) and line $\Delta t = 120$ s in Fig. 12(k)), the fault locks again.

To obtain the Δ CFS threshold of induced slip on critical stressed fault, we show the whole hydraulic-mechanical coupling process of Test 11. The fault slip initiates when all the CFS values along the entire fault exceed 0.01 MPa (from $\Delta t = 0$ s to $\Delta t = 60$ s in red curve

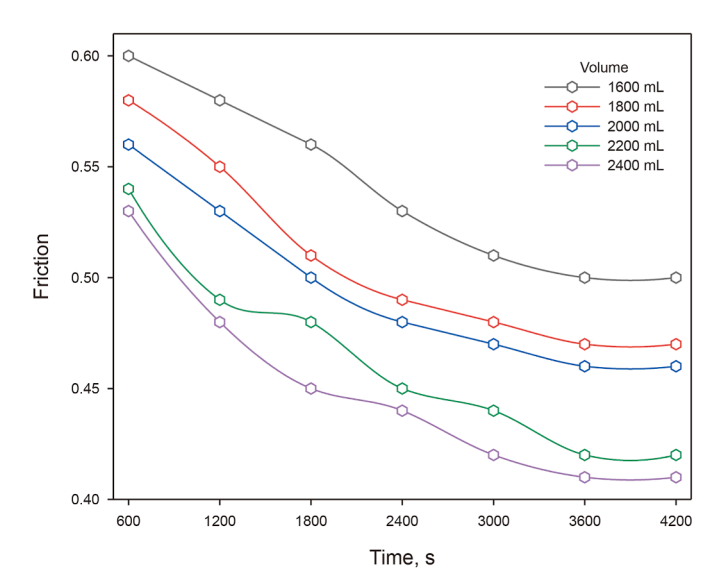


Fig. 11. The temporal evolution of fraction at different injection volumes.

of Fig. 12(m), corresponding t = 5130 s to t = 5190 s in Fig. 12(n)). In fact, the stress distribution on the fault plane is not uniform, necessitating the determination of the Δ CFS threshold based on the lowest CFS value on the original fault plane.

The samples with 45° fault are performed under two kinds of confining pressures, $\sigma_X = 0.95\sigma_{\rm crit}$ and $\sigma_X = \sigma_{\rm crit}$. The stress perturbations induced by identical injection operations almost remain consistent (e.g., the third and fourth columns in Fig. 13). In such instances, whether fault slip is predominantly governed by in-situ stress.

When injecting at injection point 3[#], the induced slip occurs on the critically stressed fault (gray line in Fig. 13(m)), but never occurs even if the stress state is close to critical stress state (blue line in Fig. 13(m)). When injecting at injection point 2[#], the induced slips occur under both two confining pressures. That is to say, when the injection point is close enough to the fault, the perturbation in normal stress and shear stress becomes significant enough to trigger induced fault slip at uncritical stress state (Fig. 13 (a)-(e), (i), and (m)). With the increase in distance between injection point and fault in the direction of maximum horizontal principal stress, the stress perturbation on the faults decreases gradually so that the fault no longer slips at uncritical stress state. And even for the critically stressed fault, the scale of induced slip decreases with the increase in distance between injection point and fault (red line and gray line in Fig. 13(m)). Same as the results of 30° fault tests, fault slip initiates when all the CFS values along the entire fault exceed 0.01 MPa (from $\Delta t = 0$ s to $\Delta t = 100$ s in the red curve of Fig. 13(m), corresponding t = 5080 s to t = 5180 s in Fig. 13(n)).

5. Discussion

5.1. σ_1/σ_3 on critical fault plane

The fluctuations of the σ_3 curve are insignificant (Fig. 8). So, we neglect the perturbation of σ_3 on the fault plane, which corresponds to the vertical stress being determined only by depth. Moreover, the stress concentration of σ_1 on the fault plane is assumed to be K(K>1). Thus, the Eqs. (1) and (2) modified to Eqs. (7) and (8),

$$\sigma_{\rm n} = \frac{K\sigma_1 + \sigma_3}{2} + \frac{K\sigma_1 - \sigma_3}{2} \cos 2\left(\frac{\pi}{2} - \alpha\right) \tag{7}$$

$$\tau = \frac{K\sigma_1 - \sigma_3}{2} \sin 2\left(\frac{\pi}{2} - \alpha\right) \tag{8}$$

Combining Eqs. (3), (7) and (8), the maximum crustal stress difference (σ_1/σ_3) can be expressed

$$\frac{\sigma_{1}}{\sigma_{3}} = \frac{\mu \left[1 - \cos 2\left(\frac{\pi}{2} - \alpha\right) \right] + \sin 2\left(\frac{\pi}{2} - \alpha\right)}{K \left[\sin 2\left(\frac{\pi}{2} - \alpha\right) - \mu - \mu \cos 2\left(\frac{\pi}{2} - \alpha\right) \right]} - \frac{2\mu p + 2C}{K\sigma_{3} \left[\sin 2\left(\frac{\pi}{2} - \alpha\right) - \mu - \mu \cos 2\left(\frac{\pi}{2} - \alpha\right) \right]} \tag{9}$$

Using the formula in the research of Hu et al. (2018), the calculated results of σ_1/σ_3 can not reflect the influence of dip on fault slip (gray line in Fig. 14). Without considering the stress concentration (Jaeger et al., 2007), the difference between the calculated result and the real value is too large (black line in Fig. 14). The accuracy of the results calculated using Eq. (7) (K= actual value) is significantly higher (red line in Fig. 14). Obviously, the approximation between the actual stress and the critical stress will be underestimated, if the stress concentration coefficient is not considered.

5.2. Shear stress drop

The difference between the initial shear stress (τ_1) and final shear stress (τ_2) on a fault before and after a fault slip is defined as the shear stress drop ($\Delta\tau$), serves as a fundamental parameter for quantifying the source scale, being a function of the total fault slip during the fault slip rupture (Allmann and Shearer, 2009). The debate about the evolution tendency of shear stress drop for small fault slip has always existed. One perspective posits that stress drop escalates with increasing fault slip scale (Hardebeck and Aron, 2009), while others argue that the stress drop for small fault slip remains essentially constant (Abercrombie, 2015). In our tests, the evolution in shear stress experiences a sequence process of increasing, decreasing, remaining stable, and subsequent increasing (as shown in Fig. 15(a) and (b)), aligning with the $\Delta\tau$ model proposed by Yamashita (1976) (Fig. 15(c)). The results provide a laboratory support for the former.

In Test 7, the average stress drop in the middle of the fault is 0.15 MPa, which is smaller than that at the edge (0.18 MPa). In Test 8, the former is 0.14 MPa, and the latter is 0.32 MPa. This is because the stress concentration at the edge of the fault is more obvious before fault slip. After fault slip, the energy accumulated in the fault is released, and the stress at each location becomes closer. Therefore, the stress drop at the edge of the fault is greater than that in the middle. The sliding distance of Tests 7 and 8 are 0.018 and 0.26 mm, respectively, the ratio is 0.07. Given that seismic moment (M_0) is the product of shear modulus (G), sliding distance (D), and rupture area (A), assuming constancy in G and G in the two tests, the moment magnitude ratio is equal to 0.07. Meanwhile, the G0 ratio of the two tests is about 0.53 (0.18 MPa/0.34 MPa). The results are highly consistent with the finding that G1 increases with G1 and satisfies the relation G2 (Mayeda and Walter, 1996).

5.3. Friction behavior

As previously mentioned, the friction of fault plane is a function of water absorption and time, when injecting upon permeable

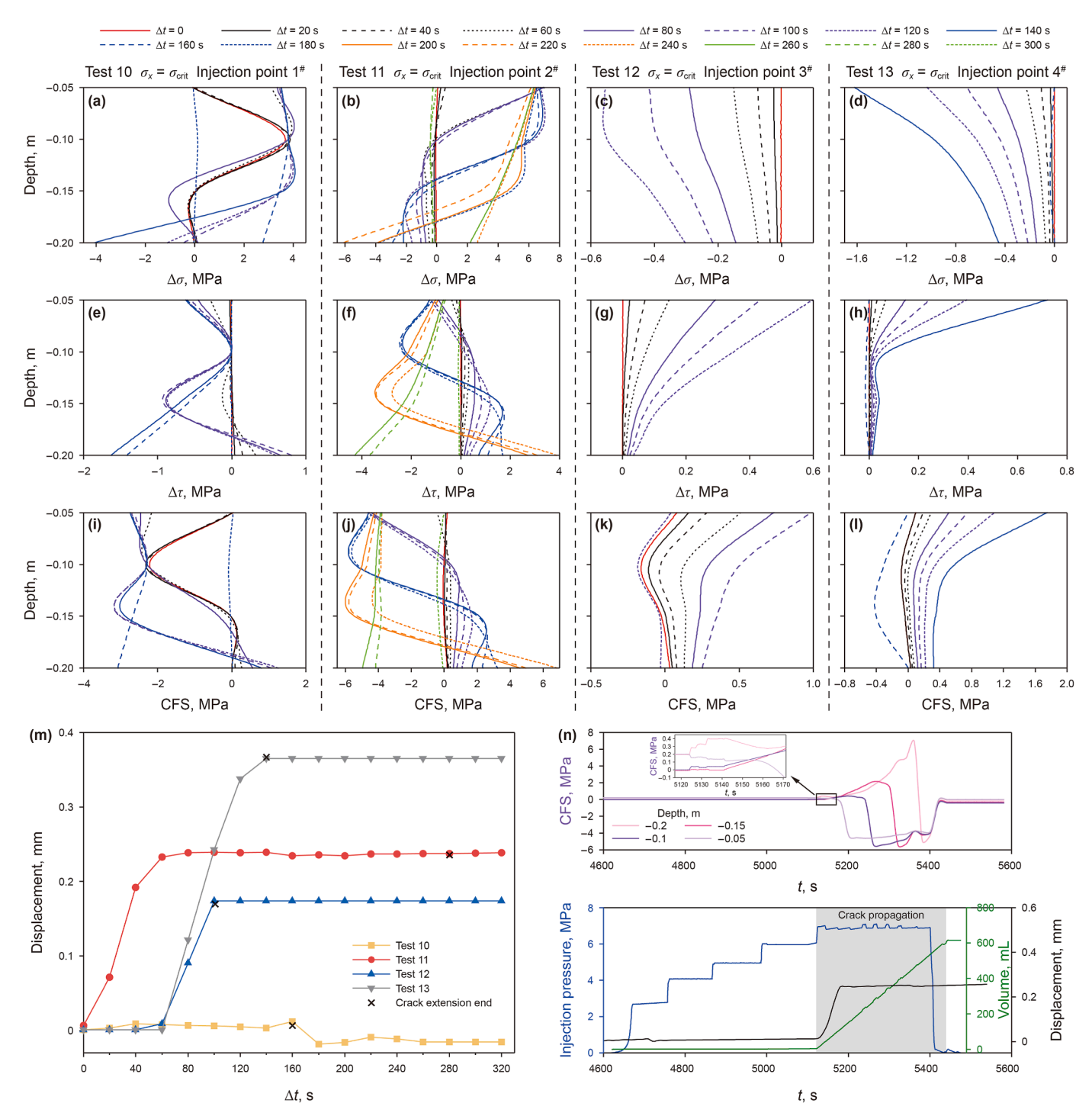


Fig. 12. Response on 30° faults. (a)–(l) Temporal evolution of stresses along the fault: (a)–(d) normal stress, (e)–(h) shear stress, (i)–(l) CFS. (m) Temporal evolution of slip. (n) Temporal evolution of all measurements, while the injection point coordinate is (0.50 m, 0.25 m, 0.30 m).

faults. When injecting upon impermeable faults, a "water film" forms between the hanging wall and the fault plane, the friction of the fault plane is difficult to measure directly. To estimate and describe the true friction, we employ the method of Guglielmi et al. (2015), which postulates that the relationship $\tau = \mu^*\sigma_{\rm eff}$ holds for each infinitesimal time interval following the onset of fault slip, disregarding viscous forces associated with fluid dynamics. Guglielmi's formula is expressed as follows:

$$\mu = \mu_0 \pm 0.05 + \ln\left(\frac{V_s}{V_0}\right), V_0 = 10^{-7} \text{m/s}$$
 (10)

where the undetermined coefficient a stands for rate dependency; V_s is the slip rate, m/s. The estimation process comprises three primary steps: First, we partition the data into intervals of 20 s and compute the average slip rate. Second, we calculate the friction as

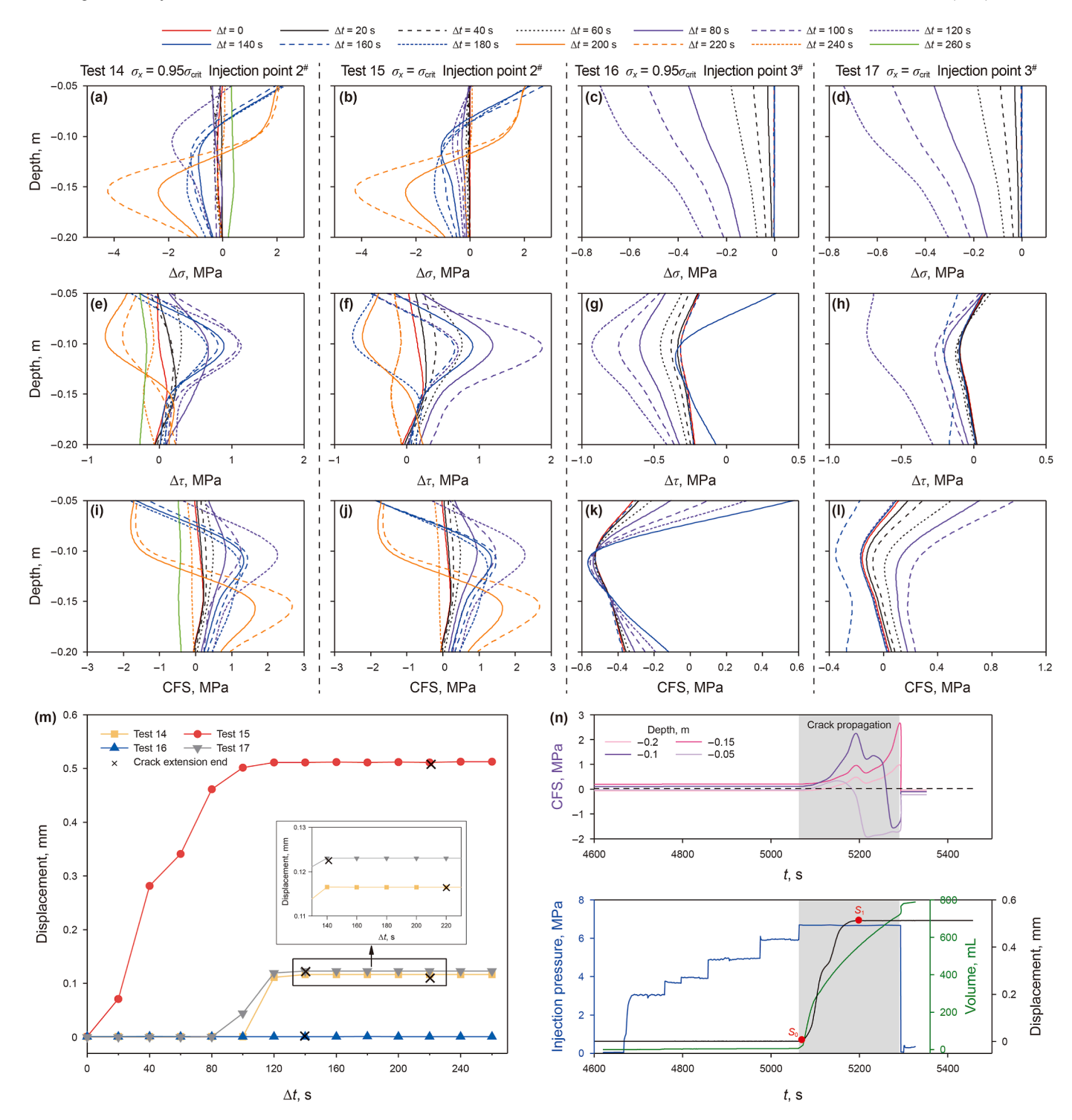


Fig. 13. Response on 45° faults. (a)–(l) Temporal evolution of stresses along the fault: (a)–(d) normal stress, (e)–(h) shear stress, (i)–(l) CFS. (m)Temporal evolution of slip. (n) Temporal evolution of all measurements, while injection hole coordinate is (0.60 m, 0.25 m, 0.25 m).

the ratio of the average effective normal stress ($\sigma_{\rm eff}$) to the average shear stress (τ). Third, we correlate the friction with the slip rate and obtain the undetermined coefficient a=0.055. The results of tests and formula suggest that fault slip behavior is primarily governed by rate-strengthening mechanisms (Fig. 16(a)). Utilizing the fitting formula, we calculate the friction at various instants. The evolution inferred from velocity measurements is in good agreement with that controlled by stress dynamics (Fig. 16(b)),

which indicates the validity of our approach and the applicability of Guglielmi's method in this specific geophysical setting.

5.4. Safe distance

Expanding the hydraulic fracturing radius to enhance extraction efficiency necessitates the precise determination of a critical distance between water injection sites and faults, which serves as

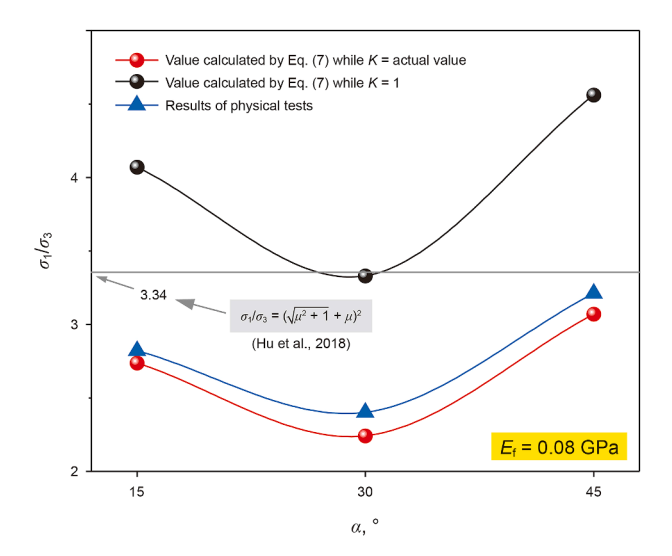


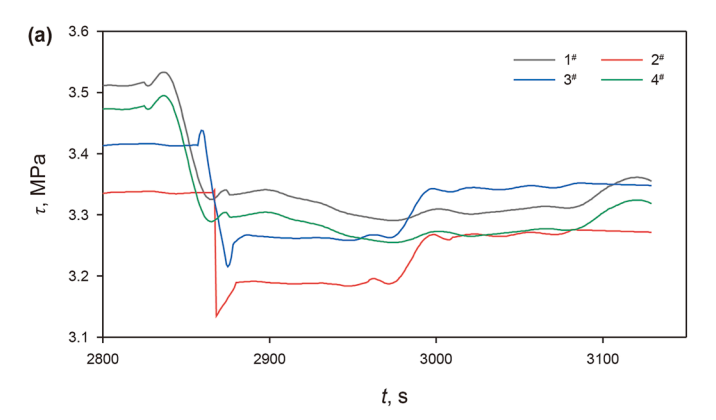
Fig. 14. Accuracy comparison.

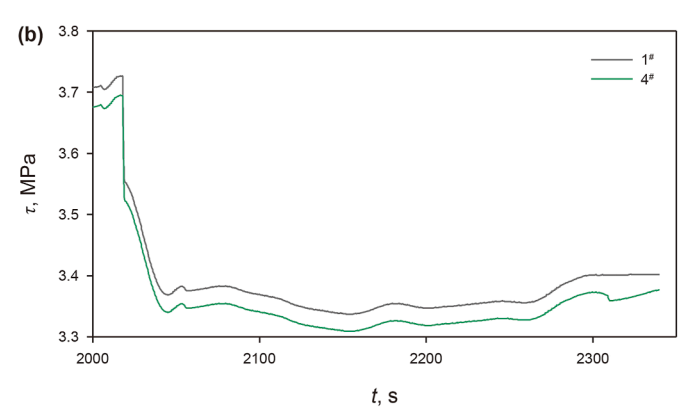
a fundamental parameter for safe and efficient operations. When the distance from injection point to faults is relatively larger (in Tests 12, 13, and 17), stress perturbation on the fault plane, injection pressure, and fracture extension length align well with the analytical model proposed by Zeng and Guo (2016). The maximum difference between measurements and the model calculations is 0.1 MPa (Fig. 17(a)–(c)). Based on the model with Δ CFS threshold of 0.1 MPa, when the injection pressure is 7 MPa (values in physical tests) and the friction of the fault plane is 0.6, the safe distance from injection point to faults in the maximum principal stress direction (d_H) must be larger than 7 times as hydraulic fracture half-length (a), meanwhile, the safe distance from injection point to faults in the vertical direction (a_V) must be larger than 5 times as hydraulic fracture half-length (Fig. 17(d)).

5.5. Operation strategies

According to the results of hydraulically connected fault tests, it is unwise to inject water near the fault for the increase in pore pressure and the decrease in fault plane friction. Secondary faults and unproven rupture surfaces near the main fault plane modify both the stress field and the fracture propagation pathways to the main fault. Therefore, HF activities near faults, even in optimal locations such as directly beneath the fault, tend to pose substantial risks.

To the hydraulically isolated faults, it is feasible that the distance from the injection well to the fault is larger than the safe distance at the critical state. In order to enhance the applicability of our results, we calculate the safe distances at different injection pressures and fault plane friction with the analytical model proposed by Zeng and Guo (2016). No significant correlation exists between safety distance and fault dip (Fig. 18(a)–(c)). The safe distance of $d_{\rm H}$ is larger than that of $d_{\rm V}$ (Fig. 18(c) and (d)). The safe distance is positively correlated with both the injection pressure and the friction. When the friction is 0.8 and the injection pressure is 100 MPa, the safe distances of $d_{\rm H}$ and $d_{\rm V}$ are 25 and 18, respectively (Fig. 18). Considering the prolonged seepage of pore water, a larger safe distance is advisable.





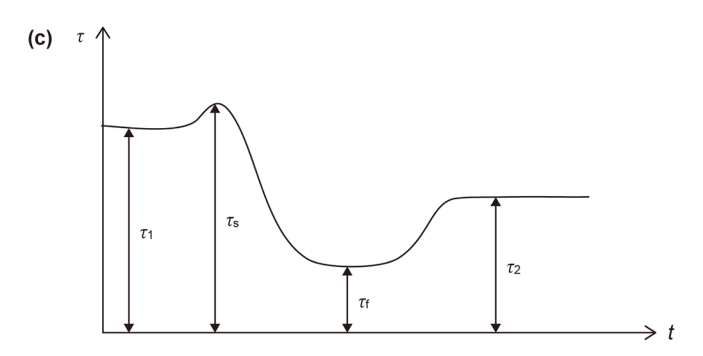


Fig. 15. Shear stress drop characteristics. Evolution curves of shear stress drops in Tests 7 (**a**) and 8 (**b**). (**c**) Shear stress drop parameters (modified from Yamashita, 1976).

According to the above analysis, we can reduce the risk of induced fault slip by implementing measures to decrease fracture propagation pressure, such as horizontal wellbore trajectory optimization (Sun et al., 2025), and pulsating hydraulic fracturing design (Peng et al., 2024).

It must be stated that this study had three important potential limitations. First, the real geological factors are more complex than our physical tests. In particular, as continuous in-situ measurements are lacking, the results of tests can only provide theoretical guidance for safety design, but can not fully represent and forecast the reality. Second, we have not discussed the situation that the fault strike intersected by σ_2 , which reduces the applicability of our results. And it has been established as the research target of our next work. Moreover, it is reasonable to assume cohesion = 0 MPa to faults which are very close to failure, or

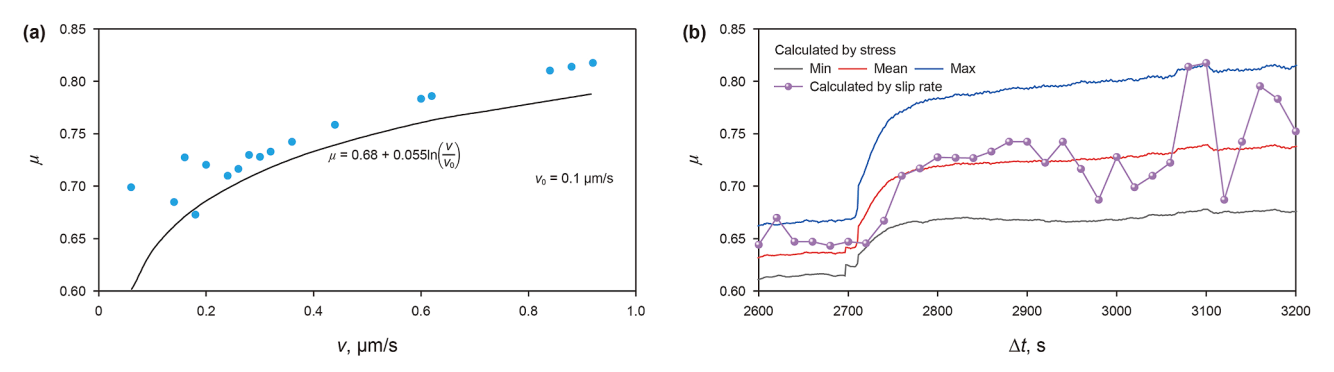


Fig. 16. (a) Relationship between slip rate and friction. (b) Evolution curve of friction.

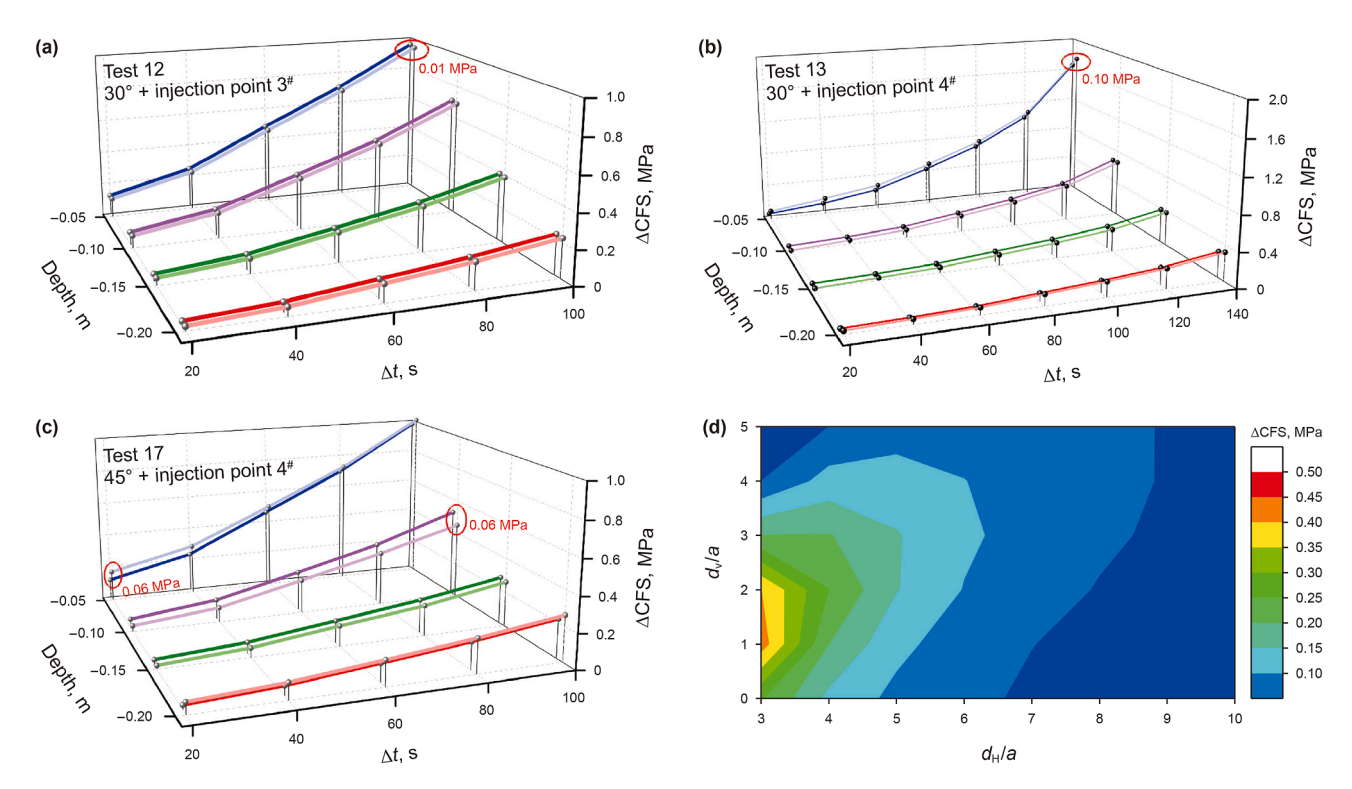


Fig. 17. Validation and application. (a)—(c) Comparison between test results (dark curve) and model calculations (light curve), the maximum differences between the test results and the model calculations are marked in red circles. (d) Safe distances.

"critically stressed" (Kettlety and Verdon, 2021; Gao et al., 2024). In fact, fault cohesion can cause underestimation of the minimum triggering threshold. That is to say, the safe distance calculated according to our findings is larger than the actual safe distance. It is desirable for the requirements of safety design.

6. Conclusions

This study optimizes the judgment formula of the maximum crustal stress difference for critical reverse fault and evaluates the impact on fault critical stress state due to the evolution of pore pressure, friction, and stress transfer caused by HF operations.

(1) The ratio of fault elasticity modulus to rock elasticity modulus governs the concentration of the maximum principal stress on the fault plane. Ignoring the stress concentration will lead to underestimation of potential risk of fault

- slip. It is advisable to set a conservative value for stress concentration in the construction scheme.
- (2) For hydraulically connected faults, induced fault slip may occur due to friction decline upon high permeable faults or/ and pore pressure diffusion upon impermeable or extremely low permeability faults, even the in-situ stress is not close to the critical state. HF operations near faults are not advisable.
- (3) For hydraulically isolated faults, induced slip can be triggered only in critical stress state by remote injection. Specially, for critical faults, induced slip is more likely to occur, when the injection pressure and/or the friction of fault plane is larger. The measures reducing the fracture propagation pressure, such as horizontal wellbore trajectory optimization and pulsating hydraulic fracturing design, are beneficial to avoid fault slip disaster.

Therefore, we suggest that a safe HF operation design requires a multi-factorial evaluation, including in-situ stress, physical

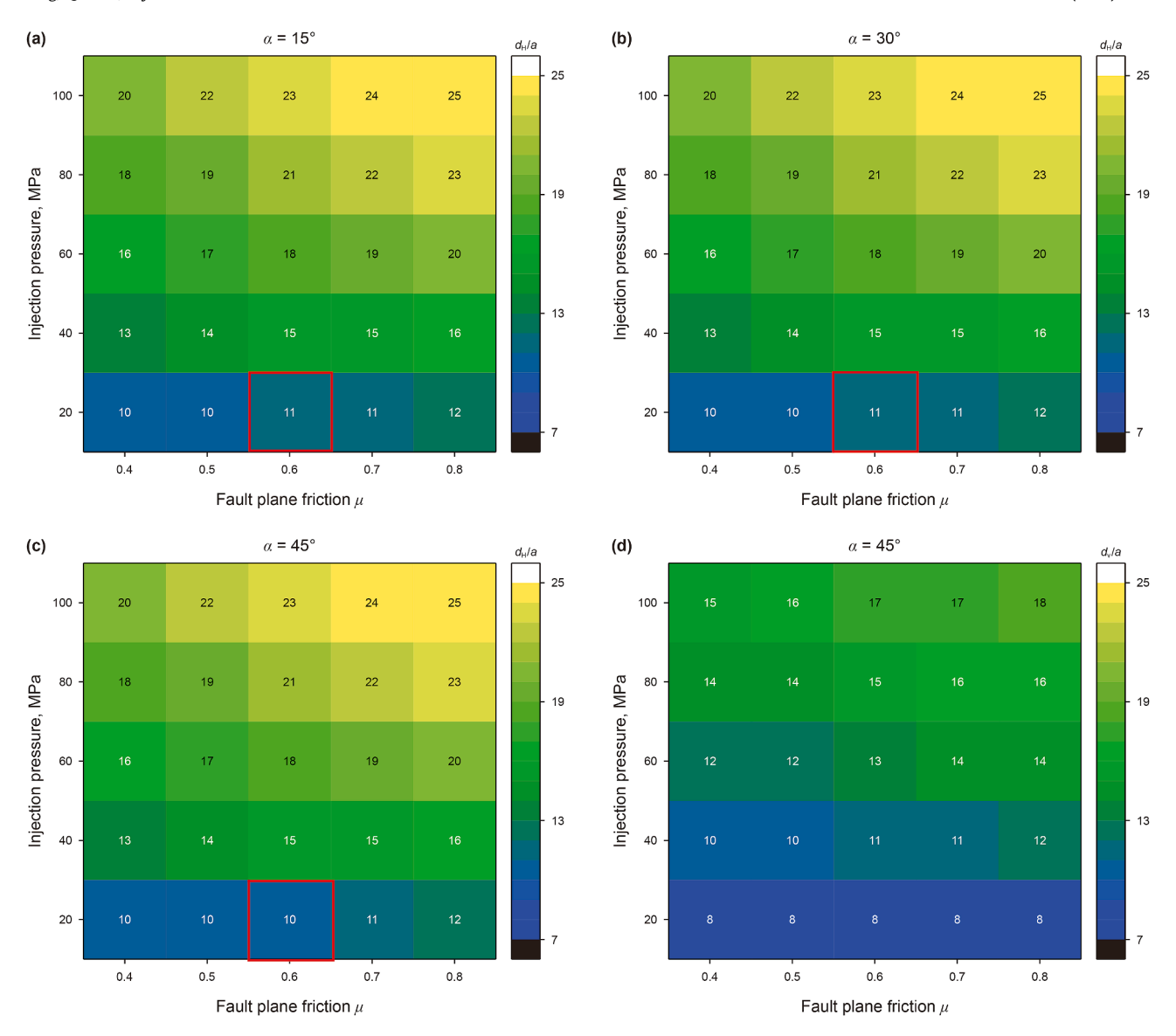


Fig. 18. The safe distances at different injection pressures and fault plane friction (the only difference in (a), (b), and (c) is framed in red).

properties of faults and reservoirs, and parameters of injection operations. The works are helpful to enable a more reliable assessment of pre- and post-injection risks and corresponding operation design.

CRediT authorship contribution statement

Xiao-Dong Wang: Writing – review & editing, Writing – original draft, Methodology, Formal analysis, Data curation, Conceptualization. Qian-Ting Hu: Supervision, Methodology, Formal analysis, Conceptualization. Yong-Jiang Luo: Writing – review & editing, Writing – original draft, Methodology, Investigation, Funding acquisition, Conceptualization. Bao-Cai Wang: Visualization, Formal analysis, Data curation. Sheng-Xian Zhao: Supervision, Conceptualization. Shao-Jun Liu: Supervision, Conceptualization. Yue Lei: Conceptualization.

Declaration of competing interest

The authors declare that they have no known competing financial interests or personal relationships that could have appeared to influence the work reported in this paper.

Acknowledgment

This research was supported by the National Natural Science Foundation of China (No.: 52274175).

References

Abercrombie, R.E., 2015. Investigating uncertainties in empirical Green's function analysis of earthquake source parameters. J. Geophys. Res. Solid Earth 120 (6), 4263–4277. https://doi.org/10.1002/2015JB011984.

Allmann, P.B., Shearer, M.P., 2009. Global variations of stress drop for moderate to large earthquakes. J. Geophys. Res. Solid Earth 114 (B1), 2008JB005821. https://doi.org/10.1029/2008JB005821.

Anyiam, U.O., Qian, J., Tan, Y., et al., 2024. Comprehensive seismic evidence for the inducing mechanism of extremely shallow 2019 Changning M_s 6.0 earthquake by solution salt mining, Sichuan Basin, China. Geology 52 (6), 441–446. https://doi.org/10.1130/G51699.1.

Atkinson, M.G., Eaton, W.D., Igonin, N., 2020. Developments in understanding seismicity triggered by hydraulic fracturing. Nat. Rev. Earth Environ. 1 (5), 264–277. https://doi.org/10.1038/s43017-020-0049-7.

Bao, X.W., Eaton, D.W., 2016. Fault activation by hydraulic fracturing in western Canada. Science 354 (6318), 1406–1409. https://doi.org/10.1126/science.aag2583.

Benson, P., Austria, D.C., Gehne, S., et al., 2020. Laboratory simulations of fluid induced seismicity, hydraulic fracture, and fluid flow. Geomech Energy Environ 24, 100169. https://doi.org/10.1016/j.gete.2019.100169.

Bhattacharya, P., Viesca, R.C., 2019. Fluid-induced aseismic fault slip outpaces porefluid migration. Science 364 (6439), 464–468. https://doi.org/10.1126/science.

- Deng, K., Liu, Y.J., Harrington, R.M., 2016. Poroelastic stress triggering of the December 2013 Crooked Lake, Alberta, induced seismicity sequence. Geophys. Res. Lett. 43 (16), 8482–8491. https://doi.org/10.1002/2016GL070421.
- Dutler, N.O., Valley, B., Amann, F., et al., 2021. Poroelasticity contributes to hydraulic-stimulation induced pressure changes. Geophys. Res. Lett. 48, e2020GL091468. https://doi.org/10.1029/2020GL091468.
- Eyre, T.S., Eaton, D.W., Garagash, D.I., et al., 2019a. The role of aseismic slip in hydraulic fracturing-induced seismicity. Sci. Adv. 5 (8), eaav7172. https://doi.org/10.1126/sciady.aav7172.
- Eyre, T.S., Eaton, D.W., Zecevic, M., et al., 2019b. Microseismicity reveals fault activation before M_w 4.1 hydraulic-fracturing induced earthquake. Geophys. J. Int. 218 (1), 534–546. https://doi.org/10.1093/gji/ggz168.
- Fan, Z., Eichhubl, P., Newell, P., 2019. Basement fault reactivation by fluid injection into sedimentary reservoirs: poroelastic effects. J. Geophys. Res. Solid Earth 124, 7354–7369. https://doi.org/10.1029/2018JB017062.
- Gao, L., Shi, X., Fan, C., et al., 2024. Fault hazard assessment in shale gas region based on seismicity and stress. Gas Sci. Eng., 205221 https://doi.org/10.1016/J. IGSCE.2024.205221.
- Ge, S., Saar, M.O., 2022. Review: Induced seismicity during geo-energy development—A hydromechanical perspective. J. Geophys. Res. Solid Earth 127 (3), e2021JB023141. https://doi.org/10.1029/2021JB023141.
- Goebel, T.H.W., Brodsky, E.E., 2018. The spatial footprint of injection wells in a global compilation of induced earthquake sequences. Science 361, 899–904. https://doi.org/10.1126/science.aat5449,1979.
- Guglielmi, Y., Cappa, F., Avouac, J., et al., 2015. Seismicity triggered by fluid injection-induced aseismic slip. Science 348 (6240), 1224–1226. https://doi. org/10.1126/science.aab0476.
- Hardebeck, L.J., Aron, A., 2009. Earthquake stress drops and inferred fault strength on the Hayward fault, East Francisco Bay, California. Bull. Seismol. Soc. Am. 99 (3), 1801–1814. https://doi.org/10.1785/0120080242.
- Hu, J., Cao, J., He, X., et al., 2018. Numerical simulation of fault activity owing to hydraulic fracturing. Appl. Geophys. 15 (3), 367–381. https://doi.org/10.1007/s11770-018-0693-6.
- Jaeger, J.C., Cook, N.G.W., Zimmerman, R.W., 2007. Fundamentals of Rock Mechanics. Chapman and Hall, London. https://doi.org/10.1017/CBO9780511735349.
- Ji, Y.L., Wang, L., Hofmann, H., et al., 2022. High-rate fluid injection reduces the nucleation length of laboratory earthquakes on critically stressed faults in granite. Geophys. Res. Lett. 49 (23). https://doi.org/10.1029/2022GL100418.
- Kemna, K.B., Roth, M.P., Wache, R.M., Harrington, R.M., Liu, Y., 2022. Small magnitude events highlight the correlation between hydraulic fracturing injection parameters, geological factors, and earthquake occurrence. Geophys. Res. Lett. 49, e2022GL099995. https://doi.org/10.1029/2022GL099995.
- Kettlety, T., Verdon, J.P., Werner, M.J., et al., 2020. Stress transfer from open inghydraulic fractures controls the distribution of induced seismicity. J. Geophys. Res. Solid Earth 125. https://doi.org/10.1029/2019JB018794.
- Kettlety, T., Verdon, J.P., 2021. Fault triggering mechanisms for hydraulic fracturing-induced seismicity from the Preston New Road, UK case study. Front. Earth Sci. 9. https://doi.org/10.3389/FEART.2021.670771.
- Kim, K.H., Ree, J.H., Kim, Y.H., et al., 2018. Assessing whether the 2017 $M_{\rm w}$ 5.4 Pohang earthquake in South Korea was an induced event. Science 360, 1007–1009. https://doi.org/10.1126/science.aat6081.
- Labuz, J.F., Zang, A., 2012. Mohr–Coulomb failure criterion. Rock Mech. Rock. Eng. 45 (6), 975–979. https://doi.org/10.1007/s00603-012-0281-7.
- Lei, X.L., Huang, D.J., Su, J.R., et al., 2017. Fault reactivation and earthquakes with magnitudes of up to Mw4.7 induced by shale-gas hydraulic fracturing in Sichuan Basin, China. Sci. Rep. 1–4, 7971. https://doi.org/10.1038/s41598-017-08557-y.
- Leng, H., Hu, J., 2024. Multi-field coupling numerical simulation on delayed reactivation of hydraulic fracturing induced faults: a case study of induced earthquakes in the Fox Creek area of Canada. Acta Seismologica Sinica 46 (3), 394–412. https://doi.org/10.11939/jass.20230070 (Abstract in English).
- Li, Q., Konstantinovskaya, E., Zhmodik, A., et al., 2023. Interaction of natural and hydraulic fractures: the impact on reservoir pressure buildup and risk of shear fault reactivation in the Upper Devonian Duvernay Formation, Fox Creek, Alberta. Geomech. Geophys. Geo. Energy Ge. Resour. 9 (1), 21. https://doi.org/ 10.1007/s40948-023-00537-z.
- Li, Y.Y., Hu, W., Wei, S.Y., et al., 2022. Influence of preexisting discontinuities on hydraulic fracture complexity a naturally fractured reservoir. Eng. Geol. 311, 106919. https://doi.org/10.1016/j.enggeo.2022.106919.
- Li, Y.Y., Hu, Y.F., Zheng, H., 2024. Influence of bedding on fracture toughness and failure patterns of anisotropic shale. Eng. Geol. 341, 107730. https://doi.org/ 10.1016/j.enggeo.2024.107730.
- Liu, H., Si, H., Xu, D.Y., et al., 2024. Laboratory investigation on slip behaviors of fault induced by cyclic confining pressure. Eng. Geol., 107575 https://doi.org/ 10.1016/j.enggeo.2024.107575.
- Liu, W., Chu, X.Y., Han, D.Y., et al., 2023. Dimensionless prejudgment criterion of coal spontaneous combustion in longwall gobs and its application. Fuel. https://doi.org/10.1016/j.applthermaleng.2023.122148.

Mayeda, K., Walter, W.R., 1996. Moment, energy, stress drop, and source spectra of western United States earthquakes from regional coda envelopes. J. Geophys. Res. Solid Earth 101 (B5), 11195–11208. https://doi.org/10.1029/96JB00112.

- Meier, M., Werner, M.J., Woessner, J., et al., 2014. A search for evidence of secondary static stress triggering during the 1992 M_w7.3 Landers California, earthquake sequence. J. Geophys. Res. Solid Earth 119, 3354–3370. https://doi.org/10.1002/2013/B010385.
- Moein, M.J.A., Langenbruch, C., Schultz, R., et al., 2023. The physical mechanisms of induced earthquakes. Nat. Rev. Earth Environ. 4 (12), 847–863. https://doi.org/ 10.1038/s43017-023-00497-8.
- Peng, Y., Wei, J.S., Zhang, Q.G., et al., 2024. Multiple damage zones around hydraulic fractures generated by high-frequency pulsating hydraulic fracturing. Pet. Sci. 21 (4), 2688–2702. https://doi.org/10.1016/J.PETSCI.2024.05.007.
- Reyes, C.M., Yusifbayov, J., van der Baan, M., 2022. Evolution of short-term seismic hazard in alberta, Canada, from induced and natural earthquakes: 2011–2020. J. Geophys. Res. Solid Earth 127, e2021JB022822. https://doi.org/10.1029/2021JB022822.
- Rezlerova, E., Brennan, J.K., Lisal, M., 2021. Methane and carbon dioxide in dualporosity organic matter: molecular simulations of adsorption and diffusion. AIChE J. 67 (3), e16655. https://doi.org/10.1002/aic.16655.
- Schultz, R., Wang, R.J., Gu, Y.J., et al., 2017. A seismological overview of the induced earthquakes in the Duvernay play near Fox Creek, Alberta. J. Geophys. Res. Solid Earth 122, 492–505. https://doi.org/10.1002/2016JB013570.
- Schultz, R., Beroza, G.C., Ellsworth, W.L., 2021. A risk-based approach for managing hydraulic fracturing-induced seismicity. Science 372, 504–507. https://doi.org/10.1126/science.abg5451, 1979.
- Sheng, M., Chu, R., Peng, Z., et al., 2022. Earthquakes triggered by fluid diffusion and boosted by fault reactivation in weiyuan, China due to hydraulic fracturing. J. Geophys. Res. Solid Earth (5), 127. https://doi.org/10.1029/ 2021/B022963.
- Sun, S.H., Gao, Y.W., Sun, X.F., et al., 2025. Intelligent optimization of horizontal wellbore trajectory based on reinforcement learning. Geoenergy Sci. Eng., 213479 https://doi.org/10.1016/J.GEOEN.2024.213479.
- Sun, Z.H., Che, M.G., Zhu, L.H., et al., 2024. Implications for fault reactivation and seismicity induced by hydraulic fracturing. Pet. Sci. 21 (2), 1081–1098. https://doi.org/10.1016/j.petsci.2023.11.022.

 Shao, C.Y., Pan, P.Z., Zhao, D.C., et al., 2020. Effect of pumping rate on hydraulic
- Shao, C.Y., Pan, P.Z., Zhao, D.C., et al., 2020. Effect of pumping rate on hydraulic fracturing breakdown pressure and pressurization rate. Rock Soil Mech. 41 (7), 2411–2421. https://doi.org/10.16285/j.rsm.2019.2145.
- Stokes, S.M., Ge, S., Brown, M.R.M., et al., 2023. Pore pressure diffusion and onset of induced seismicity. J. Geophys. Res. Solid Earth 128, e2022JB026012. https:// doi.org/10.1029/2022JB026012.
- Tan, Y.Y., Hu, J., Zhang, H.J., et al., 2020. Hydraulic fracturing induced seismicity in the southern Sichuan Basin due to fluid diffusion inferred from seismic and injection data analysis. Geophys. Res. Lett. 47, e2019GL084885. https://doi.org/ 10.1029/2019GL084885.
- Villa, V., Singh, R.P., 2020. Hydraulic fracturing operation for oil and gas production and associated earthquake activities across the USA. Environ. Earth Sci. 79 (11), 271. https://doi.org/10.1007/s12665-020-09008-0.
- Wang, B., Harrington, M.R., Liu, Y., et al., 2020. A study on the largest hydraulic-fracturing-induced earthquake in Canada: observations and static stress-drop estimation. Bull. Seismol. Soc. Am. 110 (5), 2283–2294. https://doi.org/10.1785/0120190261.
- Wang, B., Verdecchia, A., Kao, H., et al., 2021. A study on the largest hydraulic fracturing induced earthquake in Canada: numerical modeling and triggering mechanism. Bull. Seismol. Soc. Am. 111 (3), 1392–1404. https://doi.org/10.1785/ 0120200251
- Xiao, Z.M., Gu, S.T., Zhang, Y.Z., et al., 2023. An effective control method of rock burst induced by shear instability of fault structure under complicated geological conditions. Bull. Eng. Geol. Environ. 82 (4), 105. https://doi.org/ 10.1007/S10064-023-03119-1.
- Xu, J., Liu, Y.X., Yin, G.Z., et al., 2015. Development of shear-flow coupling test device for coal rock. Chin. J. Rock Mech. Eng. 34 (S1), 2987–2995. https://doi. org/10.13722/j.cnki.jrme.2014.0717 (in Chinese).
- Yamashita, T., 1976. On the dynamical process of fault motion in the presence of friction and inhomogeneous initial stress part I. J. Phys. Earth 24, 417–444. https://doi.org/10.4294/jpe1952.25.283.
- Yehya, A., Basbous, J., Maalouf, E., 2022. Analysis of the hydrogeological conditions affecting fault response to nearby hydraulic fracturing. J. Geophys. Res. Solid Earth 127 (10). https://doi.org/10.1029/2022jb024881.
- Zeng, F.H., Guo, J.C., 2016. Optimized design and use of induced complex fractures in horizontal wellbores of tight gas reservoirs. Rock Mech. Rock Eng. 49 (4), 1411–1423. https://doi.org/10.1007/s00603-015-0802-2.
- Zhang, F.Y., Wang, R.J., Chen, Y.F., et al., 2022. Spatiotemporal variations in earth-quake triggering mechanisms during multistage hydraulic fracturing in western Canada. J. Geophys. Res. Solid Earth 127 (8), e2022JB024744. https://doi.org/10.1029/2022JB024744.
- Zhang, F.Y., Chen, Y.F., Wang, R.J., et al., 2025. Integrated analysis of seismic sources and structures: understanding earthquake clustering during hydraulic fracturing. J. Geophys. Res. Solid Earth 130 (1), e2024JB030008. https://doi.org/10.1029/2024JB030008.